A mixed-dimensional finite volume method for multiphase flow in fractured porous media

Volker Reichenberger[1], Hartmut Jakobs[2],

Peter Bastian[1], Rainer Helmig[2]

We present a vertex-centered finite volume method for the fully coupled, fully implicit discretization of two-phase flow in fractured porous media. Fractures are discretely modeled as lower dimensional elements. The method works on unstructured, locally refined grids and on parallel computers with distributed memory. An implicit time discretization is employed and the nonlinear systems of equations are solved with a parallel Newton-multigrid method. Results from two-dimensional and three-dimensional simulations are presented.

Keywords: Multiphase flow; Numerical reservoir simulation; Fractured reservoir; Mixed-dimensional Finite Volume Method; Multigrid Methods.

1 Introduction

Fractures are present in many subsurface systems and can strongly influence or even dominate fluid flow and transport behavior. Because of the importance of fractured systems for secondary recovery techniques, waste disposal safety analysis and remediation techniques they have been investigated since the 1960s (Barenblatt et al., 1960; Warren and Root, 1963) and still receive considerable attention. The difficulties which arise for conceptual and numerical modeling stem from the strongly heterogeneous and anisotropic nature of the fracture-matrix system. For multiphase flow problems the behavior is much more complex than in the case of a single phase, since in the presence of two phases fractures may act as barriers or main flow paths, depending on saturation. Finally, uncertainties associated with field problems introduce difficulties into the simulation process.

Fractures appear on different length scales. We consider subsurface systems where the location and properties of the dominant fractures are known or can be estimated to good

---

[1]IWR, Universität Heidelberg, Im Neuenheimer Feld 368, 69120 Heidelberg
[2]IWS, Universität Stuttgart, Pfaffenwaldring 61, 70569 Stuttgart

agreement with the site, with the length of these fractures on the order of the size of the domain under investigation. Special consideration is given to a combined treatment of the behavior of the fluid phases in the fractures and the rock matrix, which should model accurately the interchange processes between fractures and rock matrix. This suggests a coupled approach where the fluid flow is described by a set of equations which are valid in both parts of the domain and which doesn't introduce artificial exchange terms between these parts. Instead the model incorporates a physically meaningful description of the fluid phase behavior at the media discontinuities based on the accurate treatment of the capillary pressure. We apply the extended interface conditions derived in van Duijn et al. (1995), which were originally developed for media discontinuities like lenses and layers and which are used for fractures here. This addresses the above mentioned issue of heterogeneities.

As for the problem of the anisotropic nature of fractures, we do not approach this issue from the modeling side but instead seek an appropriate discretization method. A discretization of a fractured medium domain with volumetric elements in the fractures requires a mesh which resolves the geometry of the problem. Due to the small fracture widths the resulting mesh will either consist of a very large number of elements or the mesh will contain elements with a very large aspect ratio. These elements are known to introduce difficulties into the solution behavior of iterative solvers. Our approach is to apply a mixed-dimensional finite volume discretization method which realizes fractures as lower-dimensional elements. We use one-dimensional elements for fractures in two-dimensional domains and two-dimensional fracture elements in three-dimensional domains. These elements can be used in an extension of the finite volume method of Bastian and Helmig (1999). This method is suited for unstructured grids and adaptive grid refinement as well as for efficient parallelization by domain decomposition. The nonlinear systems arising from the implicit discretization are solved by an inexact Newton method which uses multigrid for the solution of the linearized systems.

The presented method is implemented in software. The features of this software can be summarized as follows.

- Domains in 2D and 3D with unstructured, hybrid grids and adaptive grid refinement.

- Fully coupled mass-conserving vertex centered finite volume discretization.

- Physically correct treatment of capillary pressure at fracture–matrix interfaces by extended interface conditions.

- Phases can be compressible or incompressible.

- Fully implicit time discretization with selectable time stepping schemes.

- Efficient solution of the linearized systems with multigrid methods.

- Parallelization for distributed memory computers.

To the best knowledge of the authors, this combination of features in software is unique.

The organization of the rest of this paper is as follows. In the next section we present the model equations which are valid in fractures and rock matrix, and we explain the interface

conditions at the boundaries between fractures and rock matrix. Then in section 3 we present the finite volume method for the elements of mixed dimension and include some notes on implementation, parallelization and pre- and post-processing. We explain the time discretization and the nonlinear and linear solution methods. In section 4 we present results. In two dimensions a comparison of the mixed-dimensional and a standard finite volume method shows the adequacy and limitations of the method. In three dimensions, we show an application in a domain with a complex fracture network.

2 TWO-PHASE FLOW EQUATIONS

We consider an isothermal system of two phases, the wetting phase w (water in our context) and the nonwetting phase n. The phases are considered to consist of a single component each, i. e. we will not consider phase transitions. The non-wetting phase can be any non-aqueous phase liquid (NAPL) like oil or gas—the underlying equations are the same. Compressible phases are included in the model and the software implementation, which is crucial for water-gas systems. Because of the smaller density and viscosity differences the treatment of water-oil systems is numerically easier. We only present water-gas systems to prove the capability of the method. If a gas phase is referred to explicitly, we denote it with g instead of n.

Central to the derivation of the governing equations is the existence of a representative elementary volume (REV) for the fracture and the matrix. Since we treat fractures discretely, we assume that an REV exists for the rock matrix as well as for the fractures. See Berkowitz (2002) for an overview of current questions arising in fracture flow modelling.

2.1 CONSERVATION OF MASS AND DARCY'S LAW

We consider the two-phase system in a porous medium which fills the domain $\Omega \subset \mathbb{R}^d$, $d = 2, 3$. We use the set of equations also employed in Bastian and Helmig (1999) and refer to Bastian (1999) and Helmig (1997) for a more thorough description. The governing equations are the conservation of mass for each phase $\alpha = w, g$:

$$(1) \qquad \frac{\partial(\Phi \rho_\alpha S_\alpha)}{\partial t} + \nabla \cdot (\rho_\alpha \mathbf{v}_\alpha) = \rho_\alpha q_\alpha,$$

where w denotes the water phase and g denotes the NAPL phase. We assume that the effective porosity Φ only depends on position, $\Phi = \Phi(\mathbf{x})$. $S_\alpha = S_\alpha(\mathbf{x}, t)$ is the saturation of phase α and the two phases fill the pore space,

$$(2) \qquad S_w + S_n = 1.$$

$\rho_\alpha = \rho_\alpha(\mathbf{x}, t)$ is the density of phase α. For incompressible fluids ρ_α is constant, otherwise an equation of state for ideal gases is employed, $p_\alpha = \rho_\alpha RT$, with the phase pressure p_α, an individual gas constant R and the temperature T. We assume isothermal conditions. $q_\alpha = q_\alpha(\mathbf{x}, t)$ is the source term of phase α and $\mathbf{v}_\alpha$ is the Darcy velocity of phase α. The

Darcy velocity is given by a multiphase extension of Darcy's law for each phase $\alpha = w, g$,

$$(3) \qquad \mathbf{v}_\alpha = -\frac{k_{r\alpha}K}{\mu_\alpha}(\nabla p_\alpha - \rho_\alpha \mathbf{g})$$

The Darcy velocity only depends on the macroscopic phase pressure p_α. K is the tensor of absolute permeability, $k_{r\alpha}$ is the relative permeability of phase α (see next section 2.2). $\mu_\alpha = \mu_\alpha(p_\alpha)$ is the dynamic viscosity, $\mathbf{g}$ is the gravitation vector $(0, 0, -g)$, $g = 9.81 [m/s^2]$.

These equations are valid in the matrix and in the fracture if the flow is laminar in both regions. If the fracture is open, the local cubic law derived from the Hele-Shaw analog (see Bear, 1972) can be employed to define the absolute permeability for the flow of a single incompressible fluid phase: Assuming a setup of two parallel plates arranged at a distance b the averaged velocity between the plates is

$$(4) \qquad \mathbf{v} = \frac{b^2}{12}\frac{1}{\mu}\nabla h$$

with the piezometric head

$$(5) \qquad h = \frac{p}{\rho g} + z.$$

The absolute permeability is then $K = b^2/12$. Extensions to the local cubic law which incorporate fracture surface roughness can be found in Singhal and Gupta (1999).

2.2 Constitutive relations

The set of equations (1) needs to be completed with constitutive relations. We use the Brooks-Corey capillary pressure function (Brooks and Corey, 1964)

$$(6) \qquad p_c(S_w) = p_d S_e^{-\frac{1}{\lambda}}$$

which employs the effective saturation S_e of the wetting phase,

$$(7) \qquad S_e = \frac{S_w - S_{wr}}{1 - S_{wr}} \qquad S_{wr} \leq S_w \leq 1.$$

p_d is the entry pressure, S_{wr} is the residual water saturation, and λ is related to the pore size distribution: Materials with small variations in pore size have a large λ value while materials with large variations in pore sizes have small λ values. Usually λ is in the range $0.2 \leq \lambda \leq 3$.

The relative permeability functions after Brooks-Corey are

$$(8) \qquad k_{rw}(S_w) = S_e^{\frac{2+3\lambda}{\lambda}},$$

$$(9) \qquad k_{rn}(S_w) = (1 - S_e)^2(1 - S_e^{\frac{2+\lambda}{\lambda}}).$$
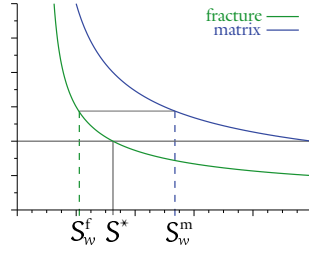
Figure 1: Brooks-Corey capillary pressure curves in rock matrix and fracture.

Across the interface between the wetting phase and the non-wetting phase a jump discontinuity occurs in the pressure, because the pressure p_n in the non-wetting phase is larger than the pressure p_w in the wetting phase. This jump is the capillary pressure p_c,

$$p_c = p_n - p_w \geq 0. \tag{10}$$

The model for the flow of a wetting fluid phase w and a non-wetting fluid phase n in a porous medium is now described by inserting (3) into (1)

$$\frac{\partial(\Phi \rho_w S_w)}{\partial t} - \nabla \cdot (\rho_w \frac{k_{rw}}{\mu_w} \mathbf{K}(\nabla p_w - \rho_w \mathbf{g})) = \rho_w q_w \quad \text{in } \Omega, \tag{11a}$$

$$\frac{\partial(\Phi \rho_n S_n)}{\partial t} - \nabla \cdot (\rho_n \frac{k_{rn}}{\mu_n} \mathbf{K}(\nabla p_n - \rho_n \mathbf{g})) = \rho_n q_n \quad \text{in } \Omega, \tag{11b}$$

This model will be used throughout the rest of this paper. The coupling of saturation and pressure by

$$S_w + S_n = 1, \quad \text{and} \quad p_n - p_w = p_c, \tag{12}$$

makes only two out of the four variables p_w, p_n, S_w, and S_n independent variables.

The model has to be complemented by appropriate boundary conditions and initial conditions which have to be chosen consistent with (12). We delay the formulation of the boundary conditions until section 3.1, where an appropriate choice of unknowns is made based on the constitutive relationships (12).

2.3 Interface conditions at Media Discontinuities

The governing equations for two-phase fluid flow in porous media are only valid if the media properties are subject to slow and smooth variation. At media discontinuities with sharp changes in properties like permeability or porosity it is necessary to introduce interface conditions which model the correct physical behavior. We adapt the approach of van Duijn et al. (1995) for the treatment of media discontinuities to the case of fractured media here.

The significant influence of the capillary pressure on the fluid flow especially at media discontinuities has been shown in laboratory experiments (Dawe et al., 1992; Kueper et al., 1989). These results indicate that it is especially important to capture the effects of the capillary forces in the description of the interface conditions since they are responsible for trapping and pooling at media discontinuities.

The partial differential equations for two-phase flow are of second order in space. An interface condition at an inner boundary does therefore have to consist of two conditions. The first condition is fluid conservation, so we require continuity of the flux of both phases across the interface.

For the derivation of the second condition we consider two parts of the domain, a fracture Ω^f and the matrix Ω^m. (The derivation is the same if we consider lenses or layers of different materials.) We assume a mobile wetting phase in both matrix and fracture, hence we require that p_w is continuous across the fracture-matrix interface Γ. The absolute permeabilities in their respective domains are

$$(13) \qquad K(\mathbf{x}) = \begin{cases} K^f(\mathbf{x}) & \text{if } \mathbf{x} \in \Omega^f, \\ K^m(\mathbf{x}) & \text{if } \mathbf{x} \in \Omega^m. \end{cases}$$

Accordingly, the porosity Φ depends on the domain as well as the capillary pressure function $p_c(S_w)$ and the relative permeability functions $k_{r\alpha}$. The shape of the capillary pressure functions $p_c(S_w)$ is shown in figure 1.

Two assumptions are essential for our framework: We do not consider blocking fractures (e. g. fractures filled with clay) and assume that

- the absolute permeability in the matrix is smaller than the absolute permeability in the fractures, $K^m(\mathbf{x}) < K^f(\mathbf{y})$ for all $\mathbf{x}, \mathbf{y} \in \Omega$, and

- the capillary pressure function values in the matrix are larger than the capillary pressure function value in the fractures for the same saturation, $p_c^m(\mathbf{x}) > p_c^f(\mathbf{x})$ for $\mathbf{x} \in \Omega$. This implies that the entry pressure of the rock matrix is larger than the entry pressure of the fractures.

For the Brooks-Corey capillary pressure relation, the entry pressure is positive, and there is a saturation $S_w^\star$ such that continuity of the capillary pressure can only be achieved if $S_w \leq S_w^\star$. In van Duijn et al. (1995) it is shown for a one-dimensional problem that for $S_w > S_w^\star$ the capillary pressure is discontinuous and that S_w is 1 in the matrix Ω^m. Physically, if the non-wetting phase is not present (i. e. $S_w = 1$ and $S_n = 0$), then p_n is undefined and p_c (which is defined as $p_n - p_w$) is also undefined. The proposed interface condition is called extended capillary pressure condition and is

$$(14) \qquad S_w^m = \begin{cases} 0 & \text{if } S_w^f > S_w^\star, \\ (p_c^m)^{-1}\left(p_c^f(S_w^f)\right) & \text{else.} \end{cases}$$

2.4 SUMMARIZATION OF MODEL ASSUMPTIONS AND CLASSIFICATION OF THE MODEL

The model equations of the previous sections only differentiate in terms of material properties between fractures and matrix. This is different than in the classical approach to fracture modeling by double porosity models (Barenblatt et al., 1960; Warren and Root, 1963), where different equations are valid in the different regions and the coupling between the domains is handled by the introduction of exchange terms. Different exchange terms have been proposed (Kazemi, 1969), but the displeasing introduction of an additional modeling parameter remains. Other extensions are multi-porosity models which extend the model by differentiating between two or more matrix species with different permeabilities, or the dual-permeability models of Hill and Thomas (1985); Clemo and Smith (1989), which considers the rock matrix not only as a storage term but allow for transmissivity in the matrix. A mathematical analysis of the double-porosity model was given in Arbogast (1989), Arbogast et al. (1990), Arbogast et al. (1991). The derivation can be found for single-phase fluids in Allaire (1997) and for two-phase flow in Bourgeat (1997). Computational aspects are considered in Arbogast (1997).

Double-porosity and double permeability models fall into the class of *equivalence models* and have mostly been employed for problems with periodic fracture networks. An alternative approach is the modeling of fractures with lower dimensional elements (sometimes called shell elements). This concept has been applied for the numerical simulation of fracture networks which neglect the influence of the matrix altogether and only model fluid flow in the fracture network. Apart from this approach, which is only justified for rocks with very small matrix conductivity, there have been finite element models which employ elements of different dimensionality. The term *discrete model* can be found in the literature for both approaches; to distinguish both the former is also called *discrete fracture network model*. The combination of discrete fracture network models with a continuum model is also known as the *hybrid model*. Wilson and Witherspoon (1974) was one of the earliest papers on numerical simulation of water flow in fractured porous media. It contains two finite element models, one with two-dimensional elements for rock matrix and fractures and one model with one-dimensional elements for the fracture network which does not take the rock matrix into account. Gureghian (1975) formulated a finite element model in three space dimensions with tetrahedral elements in the rock matrix and triangular elements in the fractures; a similar approach is presented in Baca et al. (1984) and in Eaton and Bixler (1987). The approach of element types of different dimension is also pursued in Woodbury and Zhang (2001); Sudicky and McLaren (1998).

The investigation of unsaturated flow received less attention in the past. J. S. Y. Wang and T. N. Narasimhan (1985) modeled unsaturated flow with a discrete fracture approach. Berkowitz et al. (1988) considered solute transport in a fractured porous medium with discrete fractures modeled by one-dimensional equations and the matrix modeled by two-dimensional equations, coupled by exchange terms. In Helmig (1993) mixed-dimensional elements were employed for two-phase flow; see also ROCKFLOW (1986–2003).

We consider the lack of an exchange term between fractures and rock matrix in the discrete model to be an important conceptual advantage of our method.

The assumptions which are imposed on the model can be summarized as follows.

1. We assume that fracture width is orders of magnitude smaller than the fracture length. Fractures are of essentially planar geometry, with an associated aperture in each point.

2. We assume that the multiphase fluid flow equations (11) are valid in the rock matrix and the fractures, i. e. the multiphase extension of Darcy's law is valid. This implies that we assume a laminar flow regime in both domains and that an REV can be found for fracture and matrix. Multi-component and non-isothermal behavior of the fluids is not considered.

3. The absolute permeability of the fractures is larger than the absolute permeability of the rock matrix. Fractures may be open or filled, but we do not consider blocking fractures.

4. Relative permeability functions and capillary pressure functions exist for fractures and matrix. The capillary pressure function is assumed to be strictly monotone decreasing, and we assume that the capillary pressure functions for rock and matrix do not intersect.

5. The wetting phase exists and is mobile in fractures and rock matrix.

3 Discretization with a vertex centered finite volume method

The character of multi-phase flow problems in porous media with discretely modeled fractures brings along with it some requirements for the discretization method. The complex geometry of fractured media can only be represented with unstructured grids. Consequently, the numerical scheme has to work on unstructured grids. Special attention has to be given to the fact that solutions of the multiphase flow equation (11) can exhibit sharp fronts. This suggests a locally mass conservative method since methods which are not locally mass conservative can fail to predict the correct location of shocks or sharp fronts (see Hou and LeFloch, 1994; LeVeque, 2002). Finite volume methods are suited for unstructured grids and are locally mass conservative. Properties of the finite volume method are analyzed in Bey (1998); Michev (1996).

For the time discretization we have to consider that for parabolic equations explicit methods are only stable if the time step Δt is on the order $\mathcal{O}(h^2)$ with h being the mesh size. This leads to very small time step sizes if the mesh is sufficiently fine. In order to be able to apply the method to a wide range of applications with large time steps, we choose an implicit time discretization method. The implicit time discretization generates large nonlinear systems of equations. They can be solved by inexact Newton methods. The linearized systems in the Newton method can be solved efficiently by multigrid methods, possibly accelerated by a Krylov-subspace method such as GMRES or Bi-CGSTAB.

A popular method in the context of reservoir modeling is the IMPES scheme (implicit pressure, explicit saturation), which decouples the equations into an elliptic water

phase pressure equation (which is solved implicitly) and a NAPL phase saturation equation (which is solved explicitly). The fully coupled, fully implicit approach has the advantage of being more robust and applicable to a wider range of problems. It also avoids the possibly very small time step sizes of the explicit saturation step. The stability of the fully coupled fully implicit scheme allows for larger time steps, although they should not be taken too large for accuracy reasons.

To compute a numerical solution for the two-phase flow equations, first an adequate formulation for the problem has to be found. This is done in section 3.1. Then the finite volume method is presented in sections 3.2 to 3.6. The description of the discretization method considers the domains Ω^m and Ω^f separately and then explains how a coupled treatment within the framework of conforming methods is possible. The concluding sections give an overview of the time discretization, the Newton method, the multigrid method and related implementational issues.

3.1 THE PHASE PRESSURE-SATURATION FORMULATION

As already pointed out, only two out of the four variables p_w, p_n, S_w, and S_n in the multiphase flow equations (11) can be chosen as independent variables. We choose the substitutions

$$(15) \qquad S_w = 1 - S_n, \qquad p_n = p_w + p_c(1 - S_n)$$

to obtain the (p_w, S_n)-formulation. Other choices are possible, see Helmig (1997). Despite the choice of S_n as a primary unknown, we sometimes write S_w in the following if it facilitates reading. Of course a similar exchange of p_w and p_n is not possible, because the choice of p_w as an independent variable has larger implications. Formulations based on p_w assume that the water phase exists everywhere in the domain. Because we consider problems in initially fully water-saturated domains with a residual water saturation (i. e. the water phase is never completely replaced by gas) this is the appropriate choice.

The equations now read

$$(16a) \qquad \frac{\partial(\Phi \rho_w(S_w))}{\partial t} - \nabla \cdot (\rho_w \frac{k_{rw}}{\mu_w} K(\nabla p_w - \rho_w \mathbf{g})) \qquad -\rho_w q_w = 0,$$

$$(16b) \qquad \frac{\partial(\Phi \rho_n(S_n))}{\partial t} - \nabla \cdot (\rho_n \frac{k_{rg}}{\mu_n} K(\nabla p_w + \nabla p_c(S_w) - \rho_n \mathbf{g})) - \rho_n q_n = 0,$$

where we used S_w for $1 - S_n$. We consider these equations in $(0, T) \times \Omega$. $\Omega \subset \mathbb{R}^d$, $(d = 2, 3)$ is a domain with polygonal or polyhedral boundary for $d = 2$ and $d = 3$ respectively. The equations are complemented with initial conditions and boundary conditions of Neumann or Dirichlet type on the respective boundaries $\Gamma_{\alpha n}$ and $\Gamma_{\alpha d}$

$$(17a) \qquad p_w(\mathbf{x}, 0) = p_{w0}(\mathbf{x}) \qquad\qquad S_n(\mathbf{x}, 0) = S_{n0}(\mathbf{x}) \quad \forall \mathbf{x} \in \Omega ,$$

$$(17b) \qquad p_w(\mathbf{x}, t) = p_{wd}(\mathbf{x}, t) \text{ on } \Gamma_{wd} \qquad S_n(\mathbf{x}, t) = S_{nd}(\mathbf{x}, t) \text{ on } \Gamma_{nd} ,$$

$$(17c) \qquad \rho_w \mathbf{v}_w \cdot \mathbf{n} = \phi_w(\mathbf{x}, t) \text{ on } \Gamma_{wn} \qquad \rho_n \mathbf{v}_n \cdot \mathbf{n} = \phi_n(\mathbf{x}, t) \text{ on } \Gamma_{nn}.$$

If both phases are incompressible no initial condition for p_w is required. Γ_{wd}^p should have positive measure to determine p_w uniquely.

In the following we assume the dependencies

$$\mathbf{g} = \text{constant} \tag{18}$$

$$q_\alpha = q_\alpha(\mathbf{x}, t) \tag{19}$$

$$p_c = p_c(\mathbf{x}, S_w) \tag{20}$$

$$k_{r\alpha} = k_{r\alpha}(\mathbf{x}, S_\alpha) \tag{21}$$

$$\rho_\alpha = \rho_\alpha(p_\alpha) \tag{22}$$

$$\mu_\alpha = \mu_\alpha(p_\alpha) \tag{23}$$

$$\Phi = \Phi(\mathbf{x}) \tag{24}$$

The influence of fractures on the fluid flow is included through the dependency of the quantities in equation (24) on the position, i. e. the values are different depending on whether they are evaluated in a fracture or in the rock matrix.

3.2 THE GEOMETRY OF THE PROBLEM

In the previous section the domain was only specified with respect to the shape of its boundary and without the description of fractures. We now explain the assumptions on the fracture network which are essential for the discretization method. In the following superscript m denotes entities in the volumetric rock matrix and superscript f denotes entities in the fracture network.

Let $\Omega \subset \mathbb{R}^d$ be a polygonal or polyhedral domain for $d = 2$ or $d = 3$, respectively. The domain contains a nonempty set of fractures $\{f_1, \ldots, f_F\}$. Each fracture f_i is a $(d-1)$-dimensional object—i. e. we identify each fracture with its middle surface—and each fracture f_i has a width w_i associated with it, which may be variable in the fracture. For simplicity we assume the fractures to have a planar geometry: In a two-dimensional domain the fractures are line segments and in a three-dimensional domain we assume polygonal shape of the fractures (although circular or elliptic shapes can also be treated by the method, as well as non-planar shapes). The union of the fractures constitutes the fracture network

$$\Omega^f = \bigcup_{i=1}^{F} f_i \subset \Omega. \tag{25}$$

The domain of the rock matrix Ω^m is the whole domain,

$$\Omega^m = \Omega. \tag{26}$$

This means that the domains of the fracture network and the rock matrix overlap.

3.3 THE FINITE VOLUME GRIDS AND THE DUAL GRIDS

The discretization method requires a mesh for Ω^m and Ω^f. For the volumetric mesh we consider a subdivision E_h^m of Ω^m into K elements Ω_e, $E_h^m = \{\Omega_1, \ldots, \Omega_K\}$ with $\bigcup_e \overline{\Omega_e} = \overline{\Omega}$ and $\Omega_e \cap \Omega_f = \emptyset$ for $e \neq f$. Ω_e is the open subdomain covered by the element with index e.
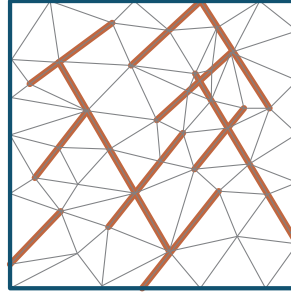
Figure 2: Example domain with fractures and mesh resolving the fracture network geometry.

h denotes the diameter of the largest element. The subdivision has to resolve the geometry of the fractures f_i, comparable to domains with inner boundaries.

Figure 2 shows an example for a two-dimensional mesh. The volumetric elements Ω_e of E_h^m are triangles or quadrilaterals in two dimensions and tetrahedra, pyramids, prisms, or hexahedra in three dimensions. Hybrid grids, i. e. grids of mixed element type are admissible, but we require that E_h^m is a triangulation: No vertex of an element lies in the interior of a side of another element.

The volumetric elements are complemented with lower dimensional elements on the fractures which are line elements for two-dimensional problems and triangles or quadrilaterals for three-dimensional problems. The fracture elements constitute a mesh $E_h^f = \{\Omega_1^f, \ldots, \Omega_{K^f}^f\}$ which is conforming with the volumetric mesh, i. e. each Ω_e is an element side or face for the two-dimensional and three-dimensional case, respectively.

The vertex centered finite volume method requires the construction of a secondary mesh B_h^m. For the volumetric mesh it is constructed by connecting element barycenters with edge midpoints as shown in figure 3 in two dimensions. In three dimensions, first the element barycenters are connected to element face barycenters and then these are connected with edge midpoints. Vertices of the grid are denoted by v_i and their corresponding coordinate vector by x_i. By construction each *control volume* contains exactly one vertex, and the control volume containing vertex v_i is denoted by b_i^m. The generation of the dual grid for the fractures happens in the same way for two-dimensional fractures. One-dimensional elements are simply divided into parts of equal length. This construction results in a conforming dual mesh for volumetric and fracture elements. The fracture dual mesh is denoted B_h^f.

The *internal skeleton* of the volumetric dual grid consists of the sides of the control volumes. The interface between control volume b and b' inside of element e is denoted by

$$(27) \qquad \gamma_{e,b,b'} = \partial\Omega_e \cap \partial\Omega_b \cap \partial\Omega_{b'} \quad \text{for } e \in E_h^m, \ b, b' \in B_h^m$$
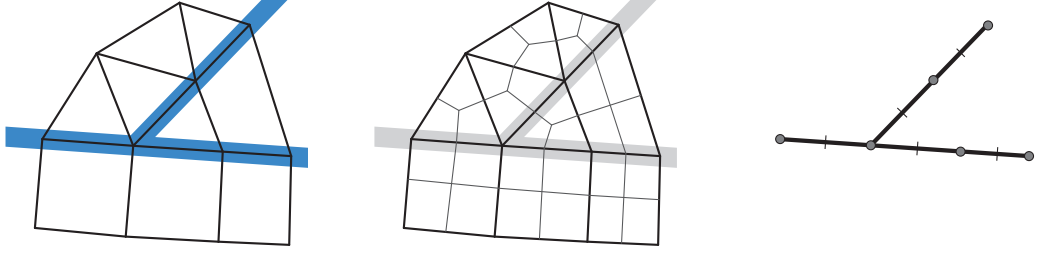
Figure 3: Mesh, dual grid and fracture elements/volumes.

and the union of all internal edges of the volumetric dual grid is denoted by

$$(28) \qquad \Gamma_{int}^m = \{\gamma_{e,b,b'} \mid e \in E_h^m, \ b, b' \in B_h^m\}.$$

For the fracture dual grid the intersection of control volume b and b' on the edge between elements e and f is

$$(29) \qquad \gamma_{e,f,b,b'} = \partial\Omega_e \cap \partial\Omega_f \cap \partial\Omega_b \cap \partial\Omega_{b'} \quad \text{for } e, f \in E_h^f, \ b, b' \in B_h^f$$

and the union of all internal control volume intersections (which are points for one-dimensional fractures and edges for two-dimensional fractures) of the fracture dual grid is denoted by

$$(30) \qquad \Gamma_{int}^f = \{\gamma_{e,f,b,b'} \mid e, f \in E_h^f, \ b, b' \in B_h^f\}.$$

In the two-dimensional case, $\gamma_{e,f,b,b'}$ is already determined uniquely by e and f (or b and b'), but in the three-dimensional case all four are needed.

The external skeleton is the union of the element sides on the domain boundary, defined for the volumetric dual mesh and the fracture dual mesh,

$$(31) \qquad \Gamma_{ext}^m = \{\gamma_{e,b} \mid \gamma_{e,b} = \partial\Omega_e \cap \partial\Omega_b \cap \partial\Omega \text{ for } e \in E_h^m, \ b \in B_h^m\},$$

$$(32) \qquad \Gamma_{ext}^f = \{\gamma_{e,f,b} \mid \gamma_{e,f,b} = \partial\Omega_e \cap \partial\Omega_f \cap \partial\Omega_b \cap \partial\Omega \text{ for } e \in E_h^f, \ b \in B_h^f\}.$$

With each element of the skeleton we associate a fixed unit normal $\mathbf{n}$. For $\gamma \in \Gamma_{ext}^m$ and $\gamma \in \Gamma_{ext}^f$ we choose the outward unit normal. For interior sides the direction of $\mathbf{n}$ is chosen arbitrarily, but fixed—a possible choice is to let $\mathbf{n}$ point from the element with the larger index to the element with the lower index.

For any function f defined on Ω, which may be discontinuous on Γ_{int}^m and Γ_{int}^f, we define the jump of f at $\mathbf{x} \in \gamma \in \Gamma_{int}$ to be

$$(33) \qquad [v](\mathbf{x}) = \lim_{\varepsilon \to 0+} v(\mathbf{x} + \varepsilon\mathbf{n}) - \lim_{\varepsilon \to 0+} v(\mathbf{x} - \varepsilon\mathbf{n}).$$
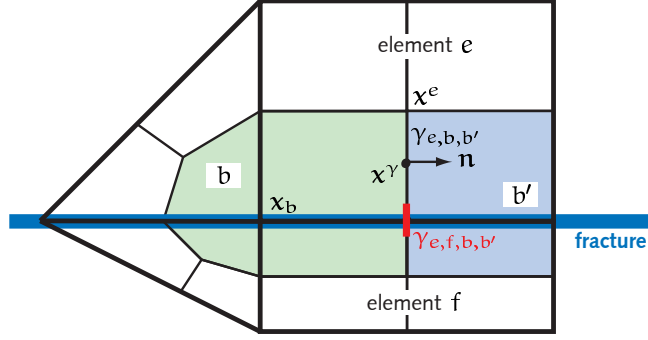
Figure 4: Notation for control volumes

3.4 Approximation spaces and weak formulation

For the discretization we introduce the standard conforming, piecewise linear finite element spaces in the matrix and fracture domain

(34) $$V_h^m = \{v \in C^0(\overline{\Omega^m}) \mid v \text{ is linear on } \overline{\Omega}_e \in E_h^m\},$$

(35) $$V_h^f = \{v \in C^0(\overline{\Omega^f}) \mid v \text{ is linear on } \overline{\Omega}_e \in E_h^f\},$$

and the non-conforming test space W_h (based on the secondary mesh)

(36) $$W_h = \{w \in L^2(\Omega^m) \mid w \text{ is constant on each } b_i \in B_h^m\},$$

(37) $$W_h^f = \{w \in L^2(\Omega^f) \mid w \text{ is constant on each } b_i^f \in B_h^f\}.$$

Figure 5 shows two basis functions for V_h^m and V_h^f. Depending on the element type (e.g. for quadrilaterals), the term *linear* has to be replaced by *multi-linear* in (34),(35) as well as in the following.

We will only describe the treatment of homogeneous Dirichlet-type boundary conditions to keep the presentation free from notational abundance. The subspaces for homogeneous Dirichlet boundary conditions for fracture and matrix and the both phases $\alpha = g, w$ are

(38) $$V_{h\alpha 0}^\tau = \{v \in V_h^\tau \mid v|_{\Gamma_{\alpha d}} = 0\},$$

(39) $$W_{h\alpha 0}^\tau = \{w \in W_h^\tau \mid w|_{\Gamma_{\alpha d}} = 0\},$$

with $\tau = m, f$. General Dirichlet boundary conditions can be treated as in Bastian (1999). In the case of inhomogeneous Dirichlet boundary conditions it is necessary to employ separate function spaces for water pressure and gas saturation, which adhere to the respective boundary conditions. These spaces can depend on time, a feature which is not explicitly mentioned. This is only a notational convenience and at all times $V_{h\alpha 0}^\tau$ and $W_{h\alpha 0}^\tau$ should be thought of as $V_{h\alpha 0}^\tau(t)$ and $W_{h\alpha 0}^\tau(t)$.
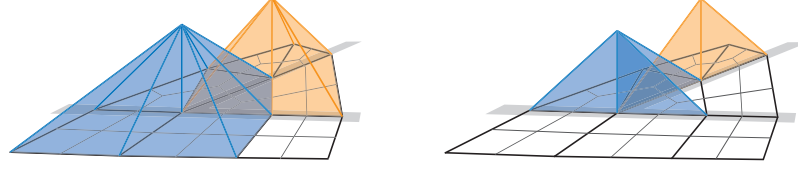
Figure 5: Basis functions for volumetric elements and fracture elements.

3.5 Discontinuous saturation spaces and projections

The phase saturations S_n and S_w are a discontinuous quantity at interfaces between media with different properties as well as at all vertices $\mathbf{v}_i \in \Omega_h^f$, because these vertices are shared by the rock matrix and the fracture network. A discontinuous saturation can not be represented by the standard conforming finite element spaces V_h^m and V_h^f so instead we choose discontinuous saturation spaces

$$(40) \qquad S_h^m = \{v \in L^2(\Omega^m) \mid v|_{\Omega_e} \text{ linear for } \Omega_e \in E_h^m\},$$

$$(41) \qquad S_h^f = \{v \in L^2(\Omega^f) \mid v|_{\Omega_e} \text{ linear for } \Omega_e \in E_h^f\}.$$

By means of the mappings Π^m and Π^f,

$$(42) \qquad \Pi^m : V_h^m \to S_h^m,$$

$$(43) \qquad \Pi^f : V_h^f \to S_h^f,$$

it is possible to formulate the discretization by the conforming finite element functions from the previous section, but to employ the correct discontinuous saturation function wherever appropriate. These mappings employ the extended interface conditions from section 2.3.

S_h^m is only continuous within elements so we define the mapping for a given $\mathbf{x} \in \Omega_e$. The values of the function

$$(44) \qquad s_h^m = \Pi^m v_h \quad v_h \in V_h^m, \, s_h \in S_h^m$$

are uniquely determined by the values of s_h in the corners of Ω_e by

$$(45) \qquad s_h(\mathbf{x}) = \Pi^m v_h(\mathbf{x}) = \sum_{i \in V(e)} S_i^e \varphi_i^m(\mathbf{x})$$

where $V(e)$ is the set of indices of the corner vertices of Ω_e and the value S_i^e at corner vertex v_i is found by

$$(46) \qquad S_i^e = \begin{cases} v(\mathbf{x}_i) & \text{if } p_c(\mathbf{x}^e, 1 - v(\mathbf{x}_i)) = p_{cmin}(\mathbf{x}_i), \\ 0 & \text{if } p_{cmin}(\mathbf{x}_i) < p_c(\mathbf{x}^e, 1), \\ 1 - S & \text{else, with } S \text{ from } p_c(\mathbf{x}^e, S) = p_{cmin}(\mathbf{x}_i). \end{cases}$$
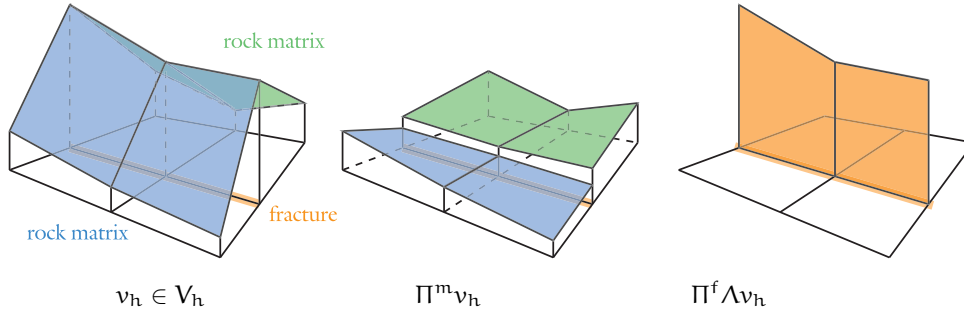
Figure 6: A function $v_h \in V_h$ and the mapping into the saturation spaces, $\Pi^m v_h$ and $\Pi^f \Lambda v_h$.

Here we employ the *minimal capillary pressure function* $p_{cmin}(\mathbf{x})$ defined as

$$(47) \qquad p_{cmin}(\mathbf{x}) = \min_{\Omega_e \in E(\mathbf{x})} p_c(\mathbf{x}^e, 1 - v(\mathbf{x}))$$

and we denote the element barycenter of element e as $\mathbf{x}^e$. $E(\mathbf{x})$ is the set of elements which contain $\mathbf{x}$ in their closure,

$$(48) \qquad E(\mathbf{x}) = \{\Omega_e \in \Omega^m \cup \Omega^f \mid \mathbf{x} \in \overline{\Omega_e}\}.$$

For fractures the same construction is employed, only that the fracture basis functions are used instead of matrix basis functions,

$$(49) \qquad s_h(\mathbf{x}) = \Pi^f v_h(\mathbf{x}) = \sum_{i \in V(e)} S_i^e \varphi_i^f(\mathbf{x}) \quad \text{for } s_h \in S_h^f, v_h \in V_h^f$$

The connection between the spaces V_h^m and V_h^f is created by the projection Λ. So far, V_h^m and V_h^f have been treated as separate spaces with separate unknowns in the vertices of the grid. The projection

$$(50) \qquad \begin{aligned} \Lambda : V_h^m &\to V_h^f \\ v_h^m &\mapsto v_h^f \end{aligned} \quad \text{with } v_h^m(\mathbf{x}) = v_h^f(\mathbf{x}) \text{ for all } \mathbf{x} \in \Omega^f.$$

is the function which maps the finite element function v_h^m defined in the matrix to the finite element function v_h^f defined in the fracture network whose values coincide in the fracture network. Figure 6 shows a function $v_h \in V_h$ and the mappings $\Pi^m v_h$ into the matrix space and $\Pi^m \Lambda v_h$ into the fracture space.

3.6 WEAK FORMULATION

The weak formulation of equations (16) for the rock matrix is found by multiplying with the test functions and integration by parts. We employ the following forms in the formu-

lation of the weak form for the rock matrix:

$$(51a) \qquad m_w^m(p_{wh}, S_{nh}, w_{wh}^m, w_{nh}^m) := \frac{\partial}{\partial t} \sum_{b \in B_h^m} \int_b \Phi \rho_w (1 - \Pi^m S_{nh}) \, d\mathbf{x}$$

$$(51b) \qquad a_w^m(p_{wh}, S_{nh}, w_{wh}^m, w_{nh}^m) := \sum_{\gamma \in \Gamma_{int}^m} \int_\gamma \rho_w \mathbf{v}_w \cdot \mathbf{n}[w_{wh}^m] \, ds$$

$$+ \sum_{\gamma \in \Gamma_{ext}^m \cap \Gamma_{wn}} \int \phi_w w_{wh}^m \, ds - \sum_{b \in B_h^m} \int_b \rho_w q_w \, d\mathbf{x}$$

$$(51c) \qquad m_n^m(p_{wh}, S_{nh}, w_{wh}^m, w_{nh}^m) := \frac{\partial}{\partial t} \sum_{b \in B_h^m} \int_b \Phi \rho_n \Pi^m S_{nh} \, d\mathbf{x}$$

$$(51d) \qquad a_n^m(p_{wh}, S_{nh}, w_{wh}^m, w_{nh}^m) := \sum_{\gamma \in \Gamma_{int}^m} \int_\gamma \rho_n \mathbf{v}_n \cdot \mathbf{n}[w_{nh}^m] \, ds$$

$$+ \sum_{\gamma \in \Gamma_{ext}^m \cap \Gamma_{nn}} \int \phi_n w_{nh}^m \, ds - \sum_{b \in B_h^m} \int_b \rho_n q_n \, d\mathbf{x}$$

The terms in m_α^m are called *accumulation term* and the terms in a_α^m are called *internal flux term*, *boundary flux term* and *source and sink term*, respectively. For the numerical evaluation of the accumulation term we employ a midpoint rule, which corresponds to the mass lumping approach in the finite element method. The Darcy velocities in the interior flux terms are evaluated with an upwind scheme. For the water phase this is for a given side $\gamma = \gamma_{e,b,b'}$

$$(52) \qquad \int_\gamma \rho_w \mathbf{v}_w \cdot \mathbf{n}[w_h] \, ds = \int_\gamma \rho_w \lambda_{w\gamma}^\star \tilde{\mathbf{v}}_w \cdot \mathbf{n}[w_h] \, ds$$

with the upwind evaluation of the mobility

$$(53) \qquad \lambda_{w\gamma}^\star = (1 - \beta)\lambda_{wh}(\mathbf{x}^\gamma) + \beta \cdot \begin{cases} \lambda_{wh}(\mathbf{x}_b) & \text{if } \tilde{\mathbf{v}}_w \cdot \mathbf{n} \geq 0 \\ \lambda_{wh}(\mathbf{x}_{b'}) & \text{else} \end{cases}$$

and the directional part of the velocity

$$(54) \qquad \tilde{\mathbf{v}}_w = -K(\mathbf{x}^e)(\nabla p(\mathbf{x}^\gamma) - \rho_w(\mathbf{x}^\gamma)\mathbf{g})$$

$\mathbf{x}^\gamma$ is the barycenter of γ and $\mathbf{x}_b$ is the grid vertex inside control volume b. The source and sink terms and the boundary flux terms are evaluated by the midpoint rule. The analogous evaluation scheme is employed for the non-wetting phase saturation. The parameter β controls the upwinding strategy. For $\beta = 1$ full upwinding is achieved, while $\beta = 0$ results in a central differencing scheme. We employ a fixed β, but adaptive choices depending on the local Peclet number are possible (Michev, 1996).

  The corresponding forms for the fracture space $m^f(\cdot, \cdot, \cdot, \cdot)$ and $a^f(\cdot, \cdot, \cdot, \cdot)$ are derived by replacing superscript m with f and using the projections Λ of p_w and S_n instead of p_w and

S_n directly.

$$(55a) \qquad m_w^f(\Lambda p_{wh}, \Lambda S_{nh}, w_{wh}^f, w_{nh}^f) := \frac{\partial}{\partial t} \sum_{b \in B_h^f} \int_b \Phi \rho_w (1 - \Lambda \Pi^f S_{nh}) \, d\mathbf{x}$$

$$(55b) \qquad a_w^f(\Lambda p_{wh}, \Lambda S_{nh}, w_{wh}^f, w_{nh}^f) := \sum_{\gamma \in \Gamma_{int}^f} \int_\gamma \rho_w \mathbf{v}_w \cdot \mathbf{n}[w_{wh}^f] \, ds$$

$$+ \sum_{\gamma \in \Gamma_{ext}^f \cap \Gamma_{wn}} \phi_w w_{wh}^f \, ds - \sum_{b \in B_h^f} \int_b \rho_w q_w \, d\mathbf{x}$$

$$(55c) \qquad m_n^f(\Lambda p_{wh}, \Lambda S_{nh}, w_{wh}^f, w_{nh}^f) := \frac{\partial}{\partial t} \sum_{b \in B_h^f} \int_b \Phi \rho_n \Pi^f \Lambda S_{nh} \, d\mathbf{x}$$

$$(55d) \qquad a_n^f(\Lambda p_{wh}, \Lambda S_{nh}, w_{wh}^f, w_{nh}^f) := \sum_{\gamma \in \Gamma_{int}^f} \int_\gamma \rho_n \mathbf{v}_n \cdot \mathbf{n}[w_{nh}^f] \, ds$$

$$+ \sum_{\gamma \in \Gamma_{ext}^f \cap \Gamma_{nn}} \phi_n w_{nh}^f \, ds - \sum_{b \in B_h^f} \int_b \rho_n q_n \, d\mathbf{x}$$

In the evaluation of these terms the lower dimension of the integrals has to be taken into account by using appropriate integral transformations and in the evaluation of the directional velocity.

Note that both w_{wh}^m and w_{nh}^m are only necessary in (51) and (55) if Dirichlet boundary conditions are present in different parts of the boundary for p_w and S_n. Additionally, w_{wh}^f and w_{nh}^f are just a notational convenience: The fracture space test functions are related to the matrix space test functions by a projection $\Xi : w_{\alpha h}^m \mapsto w_{\alpha h}^f$.

The final formulation of the coupled scheme is now found by adding the two bilinear forms: *Find $p_{wh} \in V_{hw0}$ and $S_{nh} \in V_{hg0}$ such that for all $w_{nh} \in W_{hg0}^m$, $w_{wh} \in W_{hw0}^m$ and $0 < t < T$*

$$(56) \quad m(p_{wh}, S_{nh}, w_{wh}, w_{nh}) + a(\Lambda p_{wh}, \Lambda S_{nh}, w_{wh}, w_{nh}) =$$

$$m^m(p_{wh}, S_{nh}, w_{wh}, w_{nh}) + m^f(\Lambda p_{wh}, \Lambda S_{nh}, \Xi w_{wh}, \Xi w_{nh})$$

$$+ a^m(p_{wh}, S_{nh}, w_{wh}, w_{nh}) + a^f(\Lambda p_{wh}, \Lambda S_{nh}, \Xi w_{wh}, \Xi w_{nh}) = 0.$$

3.7 TIME DISCRETIZATION

The traditional approach to the numerical solution of time-dependent partial differential equations is by the method of lines. First, a spatial discretization is applied to the problem (i. e. the finite volume method from the previous section), which leads to a system of ordinary differential equations. This system is then solved by a time differencing scheme which can be chosen from the wide range of available methods (Hairer and Wanner, 1996; Thomée, 1997). The arising systems of ordinary differential equations are stiff and should be treated by implicit methods.

We divide the time interval $(0, T)$ into discrete time steps

$$0 = t^0, \dots, t^M = T$$

of variable or fixed size and employ superscript n notation for functions (e. g. p_{wh}) and coefficient vectors (e. g. $\mathbf{S}_{nh}$) denoting values at time step t^n:

$$p_{wh}(t^n) = p_{wh}^n \text{ and } \mathbf{S}_{nh}(t^n) = \mathbf{S}_{nh}^n.$$

We employ the standard (multi-)linear nodal finite element basis; this introduces a unique relationship between the discrete functions p_{wh}, S_{nh} and their coefficient vectors $\mathbf{p}_w$ and $\mathbf{S}_n$.

The application of the finite volume discretization scheme leads to the semi-discretization

$$(57) \qquad \frac{\partial}{\partial t}\mathbf{M}_w(\mathbf{p}_w(t), \mathbf{S}_n(t)) + \mathbf{A}_w(\mathbf{p}_w(t), \mathbf{S}_n(t)) = 0,$$

$$(58) \qquad \frac{\partial}{\partial t}\mathbf{M}_n(\mathbf{p}_w(t), \mathbf{S}_n(t)) + \mathbf{A}_n(\mathbf{p}_w(t), \mathbf{S}_n(t)) = 0,$$

where $\mathbf{M}$ corresponds to m and $\mathbf{A}$ corresponds to a. The system can be written as

$$(59) \qquad \begin{pmatrix} \mathbf{M}_{ww} & \mathbf{M}_{wn} \\ \mathbf{M}_{nw} & \mathbf{M}_{nn} \end{pmatrix} \begin{pmatrix} \frac{\partial \mathbf{p}_w(t)}{\partial t} \\ \frac{\partial \mathbf{S}_n(t)}{\partial t} \end{pmatrix} + \begin{pmatrix} \mathbf{A}_w(\mathbf{p}_w, \mathbf{S}_n) \\ \mathbf{A}_n(\mathbf{p}_w, \mathbf{S}_n) \end{pmatrix} = 0$$

with the submatrices

$$(60) \qquad (\mathbf{M}_{\alpha w})_{ij} = \frac{\partial \mathbf{M}_{\alpha w,i}}{\partial \mathbf{p}_{w,j}} \qquad (\mathbf{M}_{\alpha g})_{ij} = \frac{\partial \mathbf{M}_{\alpha g,i}}{\partial \mathbf{S}_{n,j}}.$$

This results in a system of differential algebraic equations (DAE) of index 1 in implicit form. The matrix $\mathbf{M}$,

$$(61) \qquad \mathbf{M} = \begin{pmatrix} \mathbf{M}_{ww} & \mathbf{M}_{wn} \\ \mathbf{M}_{nw} & \mathbf{M}_{nn} \end{pmatrix},$$

is singular in the incompressible case. An analysis for the incompressible case shows that a discrete form of the elliptic equation has to be satisfied. This is called the *implicit constraint*. One backward Euler step guarantees the validity of the implicit constraint. Time steps computed with other choices than $\theta = 0$ in the one step θ method below do not fulfill this property, but they leave the implicit constraint fulfilled if it is satisfied in the preceding time step. For this reason, we always employ one backward Euler step as the first time step, regardless of the time differencing scheme of the subsequent steps.

The time step scheme in the one step θ notation reads: *For $n = 0, 1, \ldots, M-1$ find $\mathbf{p}_w^n$, $\mathbf{S}_n^n$ such that for $\alpha = w, n$*

$$(62) \qquad \mathbf{M}_\alpha^{n+1} + \mathbf{M}_\alpha^n + \Delta t^n \theta(\mathbf{A}_\alpha^{n+1}) + \Delta t^n(1 - \theta)(\mathbf{A}_\alpha^n) = 0$$

For $\theta = 0$ this yields the *backward* (or *implicit*) *Euler scheme*, $\theta = 1/2$ yields the *Crank-Nicholson scheme*. The implicit Euler scheme is first-order accurate and has very good stability (strongly A-stable, Hairer and Wanner (1996)), the Crank-Nicholson scheme is second order accurate but has weaker damping properties which may cause stability problems (only A-stable).

Closely related is the fractional-step-θ scheme. It consists of three sub-steps $t^n \to t^{n+\alpha} \to t^{n+1-\alpha} \to t^{n+1}$, where each sub-step k is a one-step-θ step with θ_k and Δt^k chosen as

$$\theta_1 = 2 - \sqrt{2} \qquad \Delta t^1 = (1 - \sqrt{2}/2)\Delta t = \alpha\Delta t,$$
$$\theta_2 = \sqrt{2} - 1 \qquad \Delta t^2 = (\sqrt{2} - 1)\Delta t = (1 - \alpha)\Delta t,$$
$$\theta_3 = 2 - \sqrt{2} \qquad \Delta t^3 = (1 - \sqrt{2}/2)\Delta t = \alpha\Delta t$$

The θ_i can be chosen different than above as long as $\theta_1 = \theta_3 = \theta \in (1/2, 1]$, and $\theta_2 = 1 - \theta$ holds. The fractional-step-θ scheme is of second order for $\alpha = 1 - \sqrt{2}/2$ and strongly A-stable for any $\theta \in (1/2, 1]$. The scheme possesses, other than the Crank-Nicholson scheme, the full smoothing property in case of rough initial data. Note that the sub-stepping does not result in higher computational cost since the step size Δt can be chosen three times larger than for the single-step-θ scheme.

3.8 NONLINEAR AND LINEAR SYSTEM SOLUTION

In the fully coupled, fully implicit discretization a large system of nonlinear equations has to be solved in each time step and an accurate solution of the equations is necessary, because otherwise the local mass conservation could be destroyed. The nonlinear system solution is done with an inexact Newton method, where the linearized systems arising in each step of the Newton method are solved iteratively with a multigrid method. In the first steps of the nonlinear scheme, the approximate iterative solution of the linearized systems does not deteriorate the convergence of the nonlinear solver which converges quadratically only in a close neighborhood of the solution. In a close neighborhood of the solution the defect reduction in the linear solver should be chosen adequately small. To ensure global convergence, a line search algorithm is applied in the Newton steps (see Braess, 1992).

3.8.1 INEXACT NEWTON METHOD

The discretization scheme leads to a system of nonlinear algebraic equations

$$(63) \qquad \qquad \mathbf{F}(\mathbf{z}) = \mathbf{0}$$

with a vector $\mathbf{z}$ which contains pressure and saturation unknowns,

$$(64) \qquad \qquad \mathbf{z} = (\mathbf{p}_{w,1}, \dots, \mathbf{p}_{w,N}, \mathbf{S}_{n,1}, \dots, \mathbf{S}_{n,N})^\top$$

and a vector function $\mathbf{F}$ with components

$$(65) \qquad \qquad \mathbf{F} = (\mathbf{F}_{w,1}, \dots, \mathbf{F}_{w,N}, \mathbf{F}_{n,1}, \dots, \mathbf{F}_{n,N})^\top.$$

For the one step θ scheme the components are given by

$$(66) \qquad \qquad \mathbf{F}_\alpha = \mathbf{M}_\alpha^{n+1} - \mathbf{M}_\alpha^n + \Delta t^n \theta (\mathbf{A}_\alpha^{n+1}) + \Delta t^n (1 - \theta)(\mathbf{A}_\alpha^n).$$

Dirichlet values are included in the equation and treated by inserting a trivial equation.

The linearized equations are described by the Jacobian matrix $\mathbf{J}$ of $\mathbf{F}$ at point $\mathbf{z}$,

$$(67) \qquad (\mathbf{J}(\mathbf{z}))_{ij} = \frac{\partial \mathbf{F}_i}{\partial \mathbf{z}_j}(\mathbf{z}).$$

The entries of $\mathbf{A}$ are computed by numerical differentiation,

$$(68) \qquad \frac{\partial \mathbf{J}_i}{\partial \mathbf{z}_j}(\mathbf{z}) = \frac{\mathbf{F}_i(\mathbf{z} + \Delta \mathbf{z}_j \mathbf{e}_j) - \mathbf{F}_i(\mathbf{z})}{\Delta \mathbf{z}_j} + (\mathcal{O})(\Delta \mathbf{z}_j)$$

A description of the inexact Newton algorithm can be found in Bastian (1999). In order to achieve global convergence of the method a simple line search strategy is employed in the Newton method. Initial guesses for the solution can be found from the solution of the last time step—which usually gives good initial guesses as long as the time step size is not too large—or by a hierarchical strategy, where the nonlinear system is solved on the coarsest mesh and then the solution is interpolated to the finer mesh, where this is taken as the initial guess. The process is repeated up to the finest grid level. This is an effective strategy for the first time step, where no previous solution is available. A combination of both approaches is possible and advantageous for large time steps, where the initial solution on level 0 uses the solution from the previous time step as an initial guess.

3.8.2 Multigrid solution of the linearized equations

The solution of the linearized equations typically dominates the overall runtime of fully coupled, fully implicit schemes, so an efficient solution strategy is the key to an overall efficient scheme. The fastest solvers are multigrid methods (Hackbusch, 1985), with an optimal complexity of $\mathcal{O}(N)$, where N is the number of unknowns in the system of linear equations. A further acceleration of the solution process is achieved by using the BiCGSTAB-method (van der Vorst, 1992) together with the multigrid method.

In practice, difficulties with multigrid convergence can arise from problems with discontinuities, anisotropic problems or convection dominated convection-diffusion problems. Since the interface between fractures and matrix is resolved by the coarse grid, the first problem is less severe. We employ the diagonally scaled/truncated restriction multigrid algorithm of Bastian (1999) to improve multigrid convergence in the presence of discontinuous material coefficients. The anisotropy of the fractured domain is treated by the mixed-dimensional approach, which remedies the most severe anisotropies introduced by the thin fractures. In order to achieve a robust scheme for locally refined grids, we employ the local multigrid method of Bastian et al. (1997).

The standard multigrid smoothers are not directly applicable to the Jacobian system, because some rows in the A_{ww} block of the matrix may vanish. This problem of pointwise smoothers can be circumvented by using a point-block ordering and block variants of the smoothers. This approach was used in Bastian (1999); Bastian and Helmig (1999). We order the unknowns belonging to one vertex together, resulting in an ordering

$$(69) \qquad \tilde{\mathbf{z}} = (\mathbf{p}_{w,1}, \mathbf{S}_{n,1}, \ldots, \mathbf{p}_{w,N}, \mathbf{S}_{n,N})^{\mathsf{T}}$$

which corresponds to a permutation of $\mathbf{z}$ with the permutation matrix Q,

$$(70) \qquad \tilde{\mathbf{z}} = Q\mathbf{z}.$$

Q transforms the system into the equivalent system

$$(71) \qquad \tilde{A}\tilde{\mathbf{z}} = \tilde{\mathbf{e}}$$

with

$$(72) \qquad \tilde{A} = QAQ^\mathsf{T}, \quad \tilde{\mathbf{z}} = Q\mathbf{z}, \quad \tilde{\mathbf{e}} = Q\mathbf{e}.$$

The matrix A has a block structure with $N \times N$ blocks $\tilde{A}_{ij}$ of size 2×2,

$$(73) \qquad \tilde{A} = \begin{pmatrix} \tilde{A}_{11} & \cdots & \tilde{A}_{1N} \\ \vdots & & \vdots \\ \tilde{A}_{N1} & \cdots & \tilde{A}_{NN} \end{pmatrix}.$$

Iterative schemes can now be applied because blocks $\tilde{A}_{ij}$ can only become singular at boundaries where $\rho_w \mathbf{v}_w \cdot \mathbf{n} = \phi_w$ and $S_n(\mathbf{x}, t) = 1$, but this boundary condition is not physically meaningful, since no water phase exists at points where $S_n = 1$ holds, and consequently no condition can be imposed on the water flux.

3.9 Implementation issues

The simulator is implemented based on the numerical software toolbox UG (Bastian et al., 1997). The large number of features (adaptivity on hybrid grids in 3D, parallelization) could otherwise not be achieved.

The implementation of finite volume codes often uses a loop over all elements and calculates the contribution of the dual grid skeleton from inside each element. The implementation of the presented method for rock matrix and fractures can be done based on a volumetric element code without the need to introduce the notion of lower-dimensional elements into the code, if fractures are represented as inner boundaries and if each element calculates not only the contributions from $\Gamma_{\mathrm{int}}^{\mathrm{m}}$, but also from $\Gamma_{\mathrm{int}}^{\mathrm{f}}$. Calculation of the contribution to the stiffness matrix and the defect from $\gamma_{e,f,b,b'}$ is done by element Ω_e and Ω_f which each contribute half of the value. This approach is advantageous, because it stays within the element-wise implementation paradigm and doesn't require data communication if the method is implemented on parallel computers with a domain decomposition approach.

Numerical simulations of multi-phase flow in fractured porous media rely on accurate knowledge about the material properties and domain geometry. In fractured systems the exact location of the fractures is often not known, but a good approximation of the fracture network is crucial for the simulation process. In these situations a fracture generator can be employed to generate fracture networks based on prescribed geological data. An example for a fractured domain generator is FRAC3D (Silberhorn-Hemminger, 2002), which was used to generate the example presented in section 4.2.
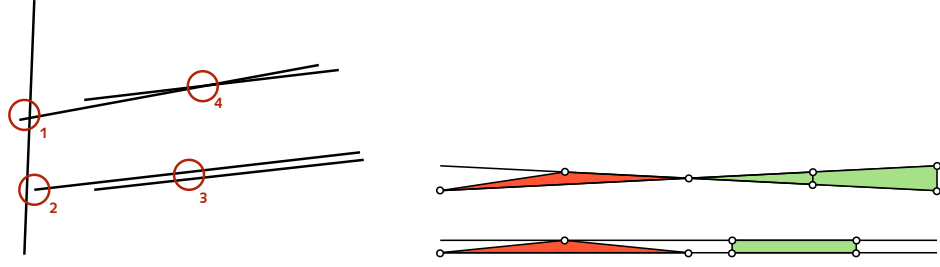
Figure 7: Four domain features which are difficult for automatic mesh generation (left) and possible elements of good quality (green) and poor quality (red) for parallel and almost parallel fractures (right).

The automatic generation of meshes has persisted as one of the most challenging tasks of the simulation process. The mesh generation for fractured porous media has to treat four configurations which are especially difficult. They are depicted in figure 7 for a two-dimensional domain, but the even more severe difficulties for three-dimensional domains can be traced back to these fundamental configurations:

1. Fracture intersections, where one fracture end protrudes only slightly from the intersection. A fine mesh is required in the vicinity of this region, which should coarsen rapidly outside this region. In three-dimensional domains, the protruding fracture end can have a "difficult" shape, e. g. a very flat triangle.

2. Almost meeting fractures, where one fracture ends in close proximity to the other. The mesh should also possess a fine resolution only near this region.

3. Parallel fractures very close to each other should be meshed with quadrilaterals in two space dimensions and with hexahedrons or prisms in three space dimensions, because they can cause the generation of elements with large inner angles.

4. Fractures intersecting at a very small angle can lead to the generation of elements with very large angles.

In both latter cases, automatic mesh generation is especially susceptible if the grid vertices are placed by a penalty functional which aims at an even distribution of vertices. In the case of parallel or almost parallel fractures this necessarily leads to large angles, where two vertices on the two fractures, placed close to each other, would produce preferable elements. This is illustrated on the right in figure 7. Even if the green quadrilateral elements are divided into triangles, their largest angles are still close to $90°$, while the largest angles of the red elements are close to $180°$. Grids for the examples in the following section were created with the mesh generator ART (Fuchs, 1999).

Finally, the visualization of fractured porous media requires rendering of values on hyperplanes and separate data sets for saturation values in fractures and matrix. Visualizations in the following section were done with OpenDX (OpenDX).
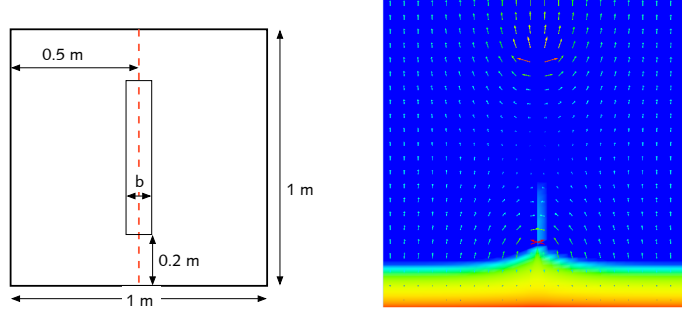
Figure 8: Sketch of the domain for the vertical water-gas flow example and S_g and $\mathbf{u}_w$ at t = 70 s.

4 EXAMPLES

Both following examples are taken from Reichenberger (2004).

4.1 VALIDATION OF THE MODEL

The first numerical experiment is chosen to assess the difference between a lower-dimensional fracture approach and a fracture with volumetric elements. The setup includes one vertical fracture inside a domain of 1[m] × 1[m]; a sketch is displayed in figure 8. The fracture is located along the line from (0.5m, 0.2m) to (0.5m, 0.8m). We consider inflow of a compressible gas phase at the south boundary.

The parameters of the simulation are artificially chosen but give a representative picture of fracture-matrix interaction. The parameters are

$$\rho_w = 1000\ [\text{kg/m}^3] \qquad \rho_g = \frac{p_n}{84149.6}\ [\text{kg/m}^3]$$

$$\mu_w = 10^{-3}\ [\text{Pa s}] \qquad \mu_g = 1.65 \cdot 10^{-5}\ [\text{Pa s}]$$

$$\Phi^f = 0.3 \qquad \Phi^m = 0.1$$

$$K^f = 10^{-8} \qquad K^m = 10^{-12}$$

$$S_{wr}^f = 0 \qquad S_{wr}^m = 0$$

$$S_{gr}^f = 0 \qquad S_{gr}^m = 0$$

$$\lambda^f = 2 \qquad \lambda^m = 2$$

$$\lambda^f = 1000\ [\text{Pa}] \qquad \lambda^m = 2000\ [\text{Pa}]$$

The fracture width b is chosen as 0.005 [m]. Boundary conditions are $S_g = p_w = 0$ on the north boundary, and Neumann boundary conditions elsewhere. At the south boundary the value of the Neumann boundary condition for the saturation is $-2.5 \cdot 10^{-5}\ [\text{kg/m}^2]$, all remaining Neumann boundary condition values are 0.
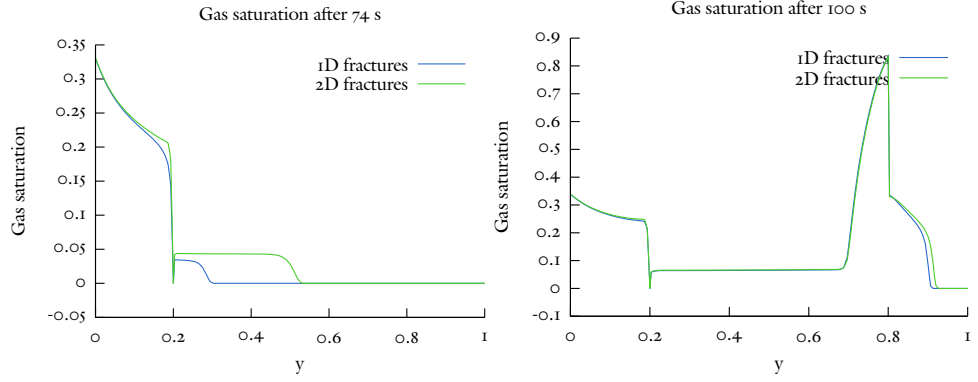
Figure 9: Comparison of the gas saturation along the vertical line at times $t = 74s$ and $t = 100s$ for $b = 0.005$ on level $l = 4$.

Without the fracture, the problem would be quasi one-dimensional, but a look at the flow field reveals how the influence of the fracture affects the solution behavior (figure 8, right). We choose a vertical fracture in order to exclude as much grid dependent phenomena as possible from the experiment.

Two different coarse grids are employed. The first grid employs the mixed dimensional finite volume method and models the fracture by one-dimensional elements. The second grid resolves the fracture with two-dimensional elements, using only quadrilateral elements. The number of elements and nodes in the grids for each refinement level is given in table 1. For the simulation we employ the backward Euler scheme with fixed time step size. The nonlinear equations are solved by the inexact Newton method with line search. The linear systems are solved with the $V(2,2)$-cycle multigrid method with ILU smoothing, accelerated by Bi-CGSTAB.

We compared the discretization schemes by plotting the value of S_g at different time

Level l	Δt [s]	one-dimensional		two-dimensional	
		#E	#N	#E	#N
2	2	153	128	221	192
3	1	561	512	825	768
4	0.5	2145	2048	3185	3072
5	0.25	8385	8192	12513	12288
6	0.5	33153	32768		
7	0.25	131841	131072		

Table 1: Time step Δt, number of elements #E and nodes #N for grids of the vertical gas flow problem.

steps along the line from $(0.5, 0)$ to $(0.5, 1)$. The time steps are chosen as $t = 74$ s, 100 s. At $t = 74$ s gas has entered the fracture and at $t = 100$ s the gas has reached the fracture end and has penetrated the matrix. In figure 9 we display the shape of the saturation curve for the two discretizations at $t = 74$ s and $t = 100$ s. This is an interesting comparison, because it compares the mixed-dimensional model with a "trusted one", the model with only two-dimensional elements.

The difference in the location of the gas front arises from the different inflow behavior between the models and is not (only) caused by numerical inaccuracies—a grid refinement study reveals that the saturation curves converge to different solutions. In the equi-dimensional model, the gas phase can enter the fracture over the lower horizontal edge of the fracture in addition to inflow of gas into the fracture over the vertical fracture edges. This difference accounts for more inflow of gas into the fractures. The example must be considered very challenging for the lower dimensional fracture model, because it introduces large difference between the mixed-dimensional and the equi-dimensional models.

Note that the total mass in the system is the same in both realizations. A contradicting impression could arise because the saturation curve resembles a one-dimensional model problem and seems to reveal that in the lower-dimensional case less mass is present. This is *not* the case—only the mass in the fracture is different. Apparently, the fracture geometry has a notable influence on the solution. Triangular or rounded shapes of the fracture ends lead to yet different solutions. The difference are small enough to be of relatively small significance when compared to other uncertainties associated with the modeling and simulation process.

We compared the results also for a domain where the fracture extends up to the south domain boundary and gas flows directly into the fracture. In this case, no differences between the saturation curves is visible. This implies that in the case of direct inflow of gas into the fractures, the differences are smaller than in the model example.

We also note that grid convergence for the mixed-dimensional model can be observed with further refinement (mesh details are given in table 1). For the equi-dimensional model, a solution on finer grids could not be obtained with reasonable time step sizes.

The differences in obtaining the solution are quite remarkable. In figure 10 we plot the number of linear multigrid cycles necessary for the simulation with 400 time steps. The systems in the lower-dimensional realization are easier to solve and require less iterations than the two-dimensional realization. The curves also reveal that the system solution only starts to get demanding when the gas has reached the fracture and the nonlinearities in the constitutive relations from the discontinuous material properties make the systems more difficult to solve.

4.2 3D EXAMPLE

We demonstrate the capability of the numerical simulator with an example of a complex fracture network. The enclosing domain for the gas-water flow simulation has a size of $12 \times 12 \times 18$ [m] and contains an interconnected fracture network with eight fractures. The domain and the initial coarse grid is shown in figure 11. Two fractures are connected to
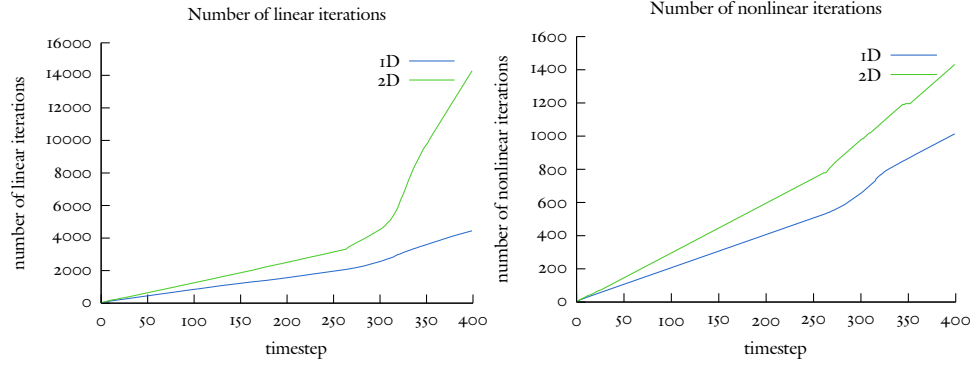
Figure 10: Linear and nonlinear iterations for vertical infiltration problem with $b = 0.005$ on level $l = 4$.
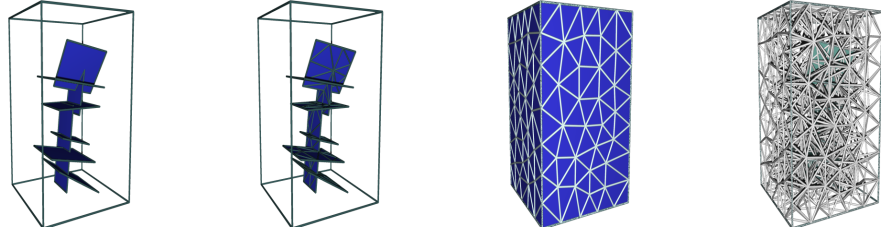

Figure 11: Domain with eight fractures and the initial grid.

the south domain boundary. It is through these fractures that the compressible gas phase enters the system.

The parameters of the simulation are (some of them taken from Wu et al. (2002))

$$\rho_w = 1000 \ [\text{kg/m}^3] \qquad \rho_g = p_g/84149.6 \ [\text{kg/m}^3]$$
$$\mu_w = 10^{-3} \ [\text{Pa s}] \qquad \mu_g = 1.65 \cdot 10^{-5} \ [\text{Pa s}]$$
$$\Phi^f = 0.084 \qquad \Phi^m = 0.114$$
$$K^f = 2.41 \cdot 10^{-12} \qquad K^m = 3.86 \cdot 10^{-15}$$
$$S_{wr}^f = 0.04 \qquad S_{wr}^m = 0.18$$
$$S_{gr}^f = 0 \qquad S_{gr}^m = 0$$
$$\lambda^f = 1.13 \qquad \lambda^m = 0.684$$
$$p_d^f = 3186.78 \ [\text{Pa}] \qquad p_d^m = 15559 \ [\text{Pa}]$$

We prescribe a hydrostatic pressure at the boundaries with $p_w = 9810$ at the north boundary. The boundary condition for the saturation is $S_g = 0$, except for the south boundary

with Neumann boundary conditions $\phi = 0$ except for the lines where the fractures intersect the domain boundary. There we set $\phi = -2.4 \cdot 10^{-4}$.

We consider two cases of grid refinement. In the case of uniform refinement 37 million elements exist on level 5; this grid does not fit into the memory of a single processor computer. The computation was carried out on the HELICS cluster (HEidelberg LInux Cluster System) consisting of AMD Athlon 1.3 GHz processors connected by a Myrinet 2000 interconnect. An alternative configuration is reached by local refinement. After one step of uniform refinement we refine only elements which contain a fracture node. The resulting grid is then suitable for typical workstation computers; the sequential results were obtained on a 1.8 GHz PowerMac G5 with 2 GB DDR SDRAM main memory. The exact number of elements and nodes is shown in table 2. The series of locally refined grids is depicted in figure 12.

The simulation uses the finite volume scheme with full upwinding and the fractional-step-θ scheme. In each Newton step a defect reduction of 10^{-5} is prescribed, and a linear defect reduction of 10^{-5}. The multigrid method uses a V(2,2)-cycle with symmetric Gauß-Seidel smoothing. The smoothing is damped with a factor 0.8. The time step size changes depending on the number of required nonlinear iterations.

Figure 13 shows the gas saturation in the fracture network and the matrix for three time steps obtained with the locally refined mesh. The gas fills the fracture rapidly and enters the rock matrix when the entry pressure is reached. The fluid velocity in the fractures depends on their orientation and is fastest for the almost vertical fractures. At fracture intersections, the gas distribution is also influenced by the fracture orientation and most gas enters into fractures with vertical or almost vertical orientation.

	uniform refinement		local refinement	
Level l	#E	#N	#E	#N
0	1.143	300	1.143	300
1	9.144	1.943	9.144	1.943
2	73.152	13.833	52.782	9.584
3	585.216	104.033	224.747	40.413
4	4.681.728	806.145	848.863	152.319
5	37.453.824	6.345.473	3.199.899	573.632

Table 2: Grids with uniform and local refinement for the 3D simulation.

#P	T [s]	Δt [s]	n_{nl}	n_{lin}	steps	T_D [s]	T_A [s]	T_L [s]	$\sum T$ [s]
16	4.5	0.125	291	1934	36	17.9	40.53	9.44	35260
256	4.5	0.0625	575	4204	72	9.19	19.77	5.01	37714

Table 3: Results from the parallel computation. All times are measured in seconds. Note that one step of the time stepping scheme consists of three one step θ sub-steps.
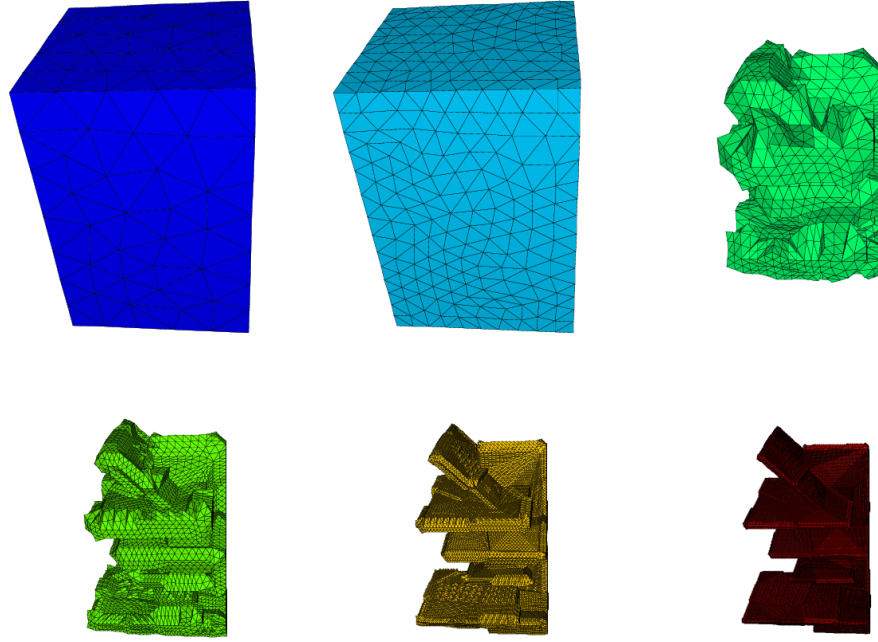
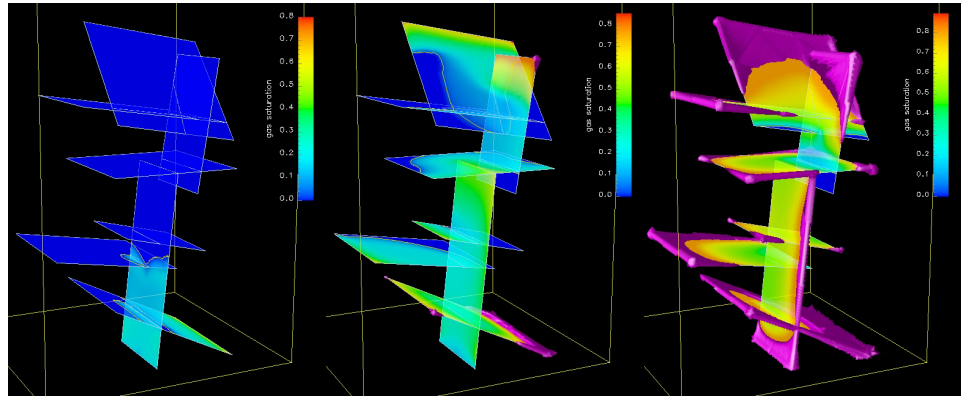Figure 12: Local grid refinement of the fractured domain.

Figure 13: Saturation in fractures and rock matrix. Saturation in the matrix corresponds to the isosurface for $S_g = 0.01$.

The parallel simulation was carried out on 16 and 256 nodes with the uniformly refined grids. With this configuration, the results in table 3 are obtained. We show the number

of processors #P, the simulated time T, the time step size Δt, the number of nonlinear solution steps n_{nl}, the number of linear solution steps n_{lin}, the number of time steps, the average execution times for nonlinear defect calculation T_D, assembling of the Jacobian T_A and one linear cycle T_L and the total computing time $\sum T$ for obtaining the solution ($n_{nl} \cdot (T_D + T_A) + n_{lin} \cdot T_L$). Note that for one refinement step the number of elements increases by a factor of eight and that the time step size is halved. This implies that for perfect speedup, the total execution time $\sum T$ would be the same for both configurations. Instead, the run time is only larger by a factor of 1.07. The additional runtime is explained by the longer time for each multigrid solution cycle and the larger number of nonlinear and linear steps necessary in the refined computation. The results also show that the method is appropriate for large Courant numbers (see also Reichenberger (2004)). Note that the time stepping scheme uses one implicit Euler step and then the fractional θ scheme, which consists of three one step θ steps. This means that when calculating the average number of Newton steps in one time step, $n_{nl}/(steps)$, one should divide the number by 3. Rather than eight Newtons steps ($575/72 \approx 8$) for the 64 processor case, the method needs less than three Newton step on average in each sub step.

5 Conclusion

We presented a fully couple, fully implicit, mixed-dimensional vertex centered finite volume method for the discretization of multiphase flow problems on unstructured hybrid grids. The discretization scheme uses multigrid methods for the fast solution of the linearized systems and it's solution is accelerated by using a parallel implementation. A comparison for a model problem in 1D showed that the differences between the mixed-dimensional discretization and a fully volumetric discretization are small. The mixed-dimensional discretization yields systems which are far easier to solve than fully volumetric discretization approach. In 3D we showed the simulation of compressible gas flow in a complex fracture network. Through local grid refinement, a suitably fine mesh can be employed for the fractures, while the problem still fits into memory of a typical desktop computer.

An extension to the case of multiphase, multicomponent would be very interesting for long-term nuclear waste repository safety analysis. The flexibility of the simulator also allows for the simulation of problems from oil reservoir engineering.

Acknowledgements

Notation

Upper case latin

B_h	Dual grid
E_h	Mesh
$\mathbf{J}$	Jacobian matrix
$\mathbf{K}$	absolute permeability [m^2]
S_α	saturation of phase α
$S_{\alpha r}$	residual saturation of phase α
V_h	conforming finite volume basis space
W_h	finite volume test space

Lower case latin

b	box volume (dual grid)
d	space dimension (2 or 3)
e, f	finite element
$\mathbf{g}$	gravity vector [m/s^2]
p_α	phase pressure, $\alpha = n, w$ [Pa]
p_c	capillary pressure [Pa]
p_d	entry pressure [Pa]
$\mathbf{n}$	normal [-]
$\mathbf{v}_\alpha$	Darcy velocity of phase α [m/s]
ν	basis function
w	test function
$\mathbf{x}$	position in $\mathbb{R}^d$]

Upper case greek

Ω	Domain
Ω^f	Domain of volumetric fractures
Ω^m	Domain of rock matrix
Ω_e	Domain of finite element e]
Λ	Projection into fracture space
Π	Mapping into saturation space
Γ_{int}	interior grid skeleton
Γ_{ext}	interior grid skeleton
$\gamma_{e,f}$	Side between elements e and f

Lower case greek

α	phase n or w
ρ	density [kg/m^3]
Φ	effective porosity [-]
p	pressure [Pa]
λ	Brooks-Corey parameter [—]
ϕ	Value of Neumann boundary condition [kg/m^2]
μ	viscosity [-]
θ	time discretization parameter
Δt	time step size

Subscript symbols

g	gas phase related quantity
n	non-wetting phase related quantity
w	wetting phase related quantity

Superscript symbols

f	A fracture related quantity
m	A rock matrix related quantity
n	time step

References

G. Allaire. One-Phase Newtonian Flow. In U. Hornung, editor, *Homogenization and Porous Media*, volume 6 of *Interdisciplinary Applied Mathematics*. Springer-Verlag, Berlin, Heidelberg, New York, 1997. ISBN 0-387-94786-8.

T. Arbogast. Analysis of the simulation of single phase flow through a naturally fractured reservoir. *SIAM J. Numer. Anal.*, 26:12–29, 1989.

T. Arbogast. Computational Aspects of Dual-Porosity Models. In U. Hornung, editor, *Homogenization and Porous Media*, volume 6 of *Interdisciplinary Applied Mathematics*. Springer-Verlag, Berlin, Heidelberg, New York, 1997. ISBN 0-387-94786-8.

T. Arbogast, J. Douglas jr., and U. Hornung. Derivation of the double porosity model of single phase flow via homogenization theory. *SIAM J. Math. Anal.*, 21:823–836, 1990.

T. Arbogast, J. Douglas jr., and U. Hornung. Modeling of naturally fractured petroleum reservoirs by formal homogenization techniques. In R. Daurtay, editor, *Frontiers in Pure and Applied Mathematics*, pages 1–19. Elsevier, Amsterdam, 1991.

R. G. Baca, R. C. Arnett, and I. P. King. Modeling of fluid flow in fractured-porous rock masses by finite-element techniques. *Int. J. Num. Meth. Fluids*, 4:337–348, 1984.

G. I. Barenblatt, I. P. Zheltov, and I. N. Kochina. Basic concepts in the theory of seepage of homogeneous liquids in fissured rocks (strata). *Journal of Applied Mathematical Mechanics (USSR)*, 24:1286–1303, 1960.

P. Bastian. Numerical Computation of Multiphase Flow in Porous Media, 1999. Habilitationsschrift.

P. Bastian, K. Birken, S. Lang, K. Johannsen, N. Neuß, H. Rentz-Reichert, and C. Wieners. UG: A flexible software toolbox for solving partial differential equations. *Computing and Visualization in Science*, 1:27–40, 1997. http://cox.iwr.uni-heidelberg.de/~ug.

P. Bastian and R. Helmig. Efficient fully-coupled solution techniques for two-phase flow in porous media. *Advances In Water Resources*, 23(1):199–216, 1999.

J. Bear. *Dynamics of Fluids in Porous Media*. Dover Publications Inc., New York, 1972.

B. Berkowitz. Characterizing flow and transport in fractured geological media: A review. *Advances in Water Resources*, 25:861–884, 2002.

B. Berkowitz, J. Bear, and C. Braester. Continuum models for contaminant transport in fractured porous formations. *Water Resources Research*, 24(8):1225–1236, 1988.

J. Bey. *Finite-Volumen- und Mehrgitter-Verfahren für elliptische Randwertprobleme*. B. G. Teubner, Stuttgart, Leipzig, 1998. ISBN 3-519-02741-0.

A. Bourgeat. Two-Phase Flow. In U. Hornung, editor, *Homogenization and Porous Media*, volume 6 of *Interdisciplinary Applied Mathematics*. Springer-Verlag, Berlin, Heidelberg, New York, 1997. ISBN 0-387-94786-8.

D. Braess. *Finite Elemente*. Springer-Lehrbuch. Springer-Verlag, Berlin, Heidelberg, New York, 1992.

R. Brooks and A. T. Corey. *Hydraulic Properties of Porous Media*, volume 3 of *Colorado State University Hydrology Paper*. Colorado State University, 1964.

T. M. Clemo and L. Smith. Solute transport in fractured media: Dual permeability models. *EOS*, 70(43), 1989.

R. A. Dawe, M. R. Wheat, and M. S. Bidner. Experimental investigation of capillary pressure effects on immiscible displacement in lensed and layered porous media. *Transport in porous media.*, 7(9):83–101, 1992.

R. R. Eaton and N. E. Bixler. Analysis of a multiphase, porous-flow imbibition experiment in a fractured volcanic tuff. In D. D. Evans, editor, *Flow and Transport through Unsaturated Fractured Rock*, pages 91–97. Geophysical Monograph 42, 1987.

A. Fuchs. *Optimierte Delaunay-Triangulierungen zur Vernetzung getrimmter NURBS-Körper*. Shaker Verlag, 1999.

A. B. Gureghian. A study by the finite element method of the influence of fractures in confined aquifers. *Soc. Pet. Eng. J.*, 15:181–191, 1975.

W. Hackbusch. *Multi-Grid Methods and Applications*. Springer-Verlag, Berlin, Heidelberg, New York, 1985.

E. Hairer and G. Wanner. *Solving ordinaray differential equations II. Stiff and differential algebraic problems*, volume 14 of *Springer Series in Computational Mathematics*. Springer-Verlag, Berlin Heidelberg New York, 2 edition, 1996. ISBN 3-540-60452-9.

R. Helmig. *Theorie und Numerik der Mehrphasenströmungen in geklüftet–porösen Medien*. PhD thesis, Institut für Strömungsmechanik und Elektronisches Rechnen im Bauwesen, Universität Hannover, Bericht Nr. 34, 1993.

R. Helmig. *Multiphase Flow and Transport Processes in the Subsurface. A Contribution to the Modeling of Hydrosystems*. Springer-Verlag, Berlin, Heidelberg, New York, 1997.

A. Hill and G. Thomas. A New Approach for Simulating Complex Fractured Reservoirs. In *Reservoir Simulation Symposium, Dallas*, 1985.

T. Y. Hou and P. G. LeFloch. Why nonconservative schemes converge to wrong solutions: Error analysis. *Mathematics of Computation*, 62(206):497–530, April 1994.

J. S. Y. Wang and T. N. Narasimhan. Hydrologic mechanisms governing fluid flow in a partially saturated fractured prous medium. *Water Resources Research*, 21(12):1861–1874, 1985.

H. Kazemi. Pressure Transient Analysis of Naturally Fractured Reservoirs. *Trans. AIME*, 256:451–461, 1969.

B. H. Kueper, W. Abbott, and G. Farquhar. Experimental Observations of Multiphase Flow in Heterogeneous Porous Media. *Journal of Contaminant Hydrology*, 5:83–95, 1989.

R. J. LeVeque. *Finite Volume Methods for Hyperbolic Problems*. Cambridge Texts in Applied Mathematics. Cambridge University Press, Cambridge, 2002. ISBN 0-521-00924-3.

I. D. Michev. *Finite volume and finite volume element methods for nonsymmetric problems*. PhD thesis, Texas A&M University, College Station, 1996.

OpenDX. The Open Source Software based on IBM's Visualization Data Explorer. `http://www.opendx.org/`.

V. Reichenberger. *Numerical Simulation of Multiphase Flow in Fractured Porous Media*. PhD thesis, IWR, Universität Heidelberg, 2004.

ROCKFLOW. *Theorie und Benutzeranleitung zum Programmsystem ROCKFLOW*. Institut für Strömungsmechanik und Elektronisches Rechnen im Bauwesen, Universität Hannover, 1986–2003.

A. Silberhorn-Hemminger. *Modellierung von Kluftaquifersystemen: Geostatistische Analyse und deterministisch-stochastische Kluftgenerierung*. PhD thesis, IWS, Universität Stuttgart, 2002.

B. B. S. Singhal and R. P. Gupta. *Applied Hydrogeology of Fractured Rocks*. Kluwer Academic Publishers, Dordrecht, Boston, London, 1999.

E. A. Sudicky and R. G. McLaren. *FRACTRAN user's guide – an efficient simulator for two-dimensional, saturated groundwater flow and solute transport in Porous or discretely fractured porous formations*. Waterloo Centre for Groundwater Research, University of Waterloo, 1998.

V. Thomée. *Galerkin finite element methods for parabolic problems*. Number 25 in Springer Series in Computational Mathematics. Springer-Verlag, Berlin, Heidelberg, New York, 1997. ISBN 3-540-63236-0.

H. A. van der Vorst. BiCGSTAB: A fast and smoothly converging variant of Bi-CG for the solution of non-symmetric linear systems. *SIAM J. Sci. Stat. Comput.*, 13:631–644, 1992.

C. J. van Duijn, J. Molenaar, and M. J. de Neef. Effects of capillary forces on immiscible two-phase flow in heterogeneous porous media. *Transport in Porous Media*, 21:71–93, 1995.

J. E. Warren and P. J. Root. The behavior of naturally fractured reservoirs. *Soc. Pet. Eng. J. (Trans AIME)*, 3(228):245–255, 1963.

C. R. Wilson and P. A. Witherspoon. Steady state flow in rigid networks of fracures. *Water Resources Research*, 10(2):328–335, 1974.

A. Woodbury and K. Zhang. Lanczos method for the solution of groundwater flow in discretely fractured porous media. *Advances in Water Resources*, 24:621–630, 2001.

Y.-S. Wu, W. Zhang, L. Pan, J. Hinds, and G. S. Bodvarsson. Modeling capillary barriers in unsaturated fractured rock. *Water Resources Research*, 38(11), 2002.